Time-of-flight flow imaging using NMR remote detection

J. Granwehr,* E. Harel, S. Han,† S. Garcia, and A. Pines
Materials Sciences Division, Lawrence Berkeley National Laboratory, and Department of Chemistry, University of California at Berkeley, Berkeley, CA 94720-1460

P. N. Sen and Y.-Q. Song‡
Schlumberger-Doll Research, 36 Old Quarry Road, Ridgefield, CT 06877
(Dated: May 6, 2005)

A time-of-flight imaging technique is introduced to visualize fluid flow and dispersion through porous media using NMR. As the fluid flows through a sample, the nuclear spin magnetization is modulated by RF pulses and magnetic field gradients to encode the spatial coordinates of the fluid. When the fluid leaves the sample, its magnetization is recorded by a second RF coil. This scheme not only facilitates a time-dependent imaging of fluid flow, it also allows a separate optimization of encoding and detection subsystems to enhance overall sensitivity. The technique is demonstrated by imaging gas flow through a porous rock.

PACS numbers: 61.43.Gt, 76.60.Pc, 83.85.Fg

NMR has become an invaluable tool for the characterization of materials owing to recent progress in instrumentation and experimental techniques [1]. In particular, the development of novel approaches to the control of spin coherence in the presence of inhomogeneous magnetic fields [2–4] and inside-out NMR hardware [5, 6] highlight the potential of NMR in field studies of natural and industrial materials. For example, inside-out NMR was recently used to study methane-hydrate growth on the sea floor at a depth of 2500 m [7]. Furthermore, NMR has been recognized as a powerful method to visualize flow in porous media as evidenced in recent reports, e.g. Ref [8–12].

One factor limiting the application of NMR for field experiments is that the sample is invariably outside the NMR instrument, causing a very poor filling factor and resulting in a low signal-to-noise ratio. This limitation can be overcome in some cases by performing the NMR experiment in two steps. Let us consider a fluid-filled porous object as an example. First, the spin manipulations by radio frequency (RF) radiation are performed on the fluid within the sample *in situ*, and then the spin magnetization is rotated onto the static magnetic field. After this (encoding) step, the fluid is removed from the sample into a highly optimized detection system to read out its longitudinal magnetization. As long as a substantial magnetic field exists along the flow path, the spin magnetization will follow the local field adiabatically, and no significant signal loss should occur en route to the detection system [13]. This idea of remote detection has been demonstrated recently to enhance the sensitivity of NMR spectroscopy and imaging [14, 15].

A natural consequence of remote detection is that the received signal is dependent on the flow pattern in the sample. Fluid from the far end of the sample during encoding will arrive later than fluid nearer to the detector, and no signal will be detected from a stagnant region that is not effectively connected to the flow field. Heterogeneity in the flow field causes some flow paths to be preferred. This can be a result of the structural heterogeneity present in some porous samples like certain rocks, where it is believed to critically determine the crude oil recovery efficiency and rate. Most importantly, such heterogeneity might not be readily determined from a pore-level structural characterization, e.g. Refs. [16–20]. Remote detection MRI has the potential to overcome many technical difficulties in high field MRI of rocks and to enable *in situ* study of flow in the field. This letter reports an experimental demonstration of this flow imaging scheme by monitoring gas flow through a porous rock.

The basic idea of remote detection NMR is illustrated in Figure 1a, which highlights the fluid flowing through a porous object. The sample is placed within the active volume of the encoding coil, and a flow system is connected to transport the fluid downstream to the detection coil. An example of an RF pulse sequence is shown in Figure 1b. During the encoding step, an RF pulse is applied using the encoding coil in the presence of a magnetic field gradient to invert the spins only within a slice of the sample. The inverted spins then flow out of the sample into the detection coil, where a train of RF pulses is applied to detect an FID signal after each pulse. The flow through the sample is characterized by the time-of-flight (TOF) of the sensor from the time of encoding to the time when it reaches the detector, allowing the entire TOF pattern to be recorded transiently.

The experimental setup is detailed elsewhere [21], and only a brief description is given here. Two independent RF probes were used for encoding and detection. Encoding was done using a commercial imaging probe (Varian Inc., Palo Alto, CA) with a cylindrical cavity through the full length. Detection was done with a home-built probe that could be inserted into the encoding probe. The coils of the two probes were placed close to each

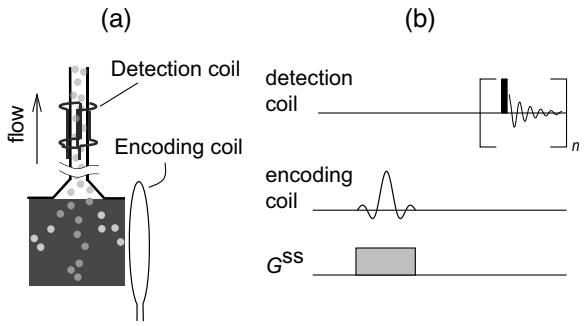

FIG. 1: Concept of remote detection NMR. (*a*) A porous sample (black square) is placed in the active volume of the encoding coil. Information is encoded as polarization of the sensor medium (gray circles), flowing out of the sample into the detection coil. (*b*) A pulse sequence for remote detection NMR. The encoding RF pulse in the presence of the field gradient G^{ss} is applied to invert the magnetization only in a slice perpendicular to the gradient direction. A train of n detection pulses is applied to measure the signal stroboscopically as the sensor medium gradually flows through the detection coil.

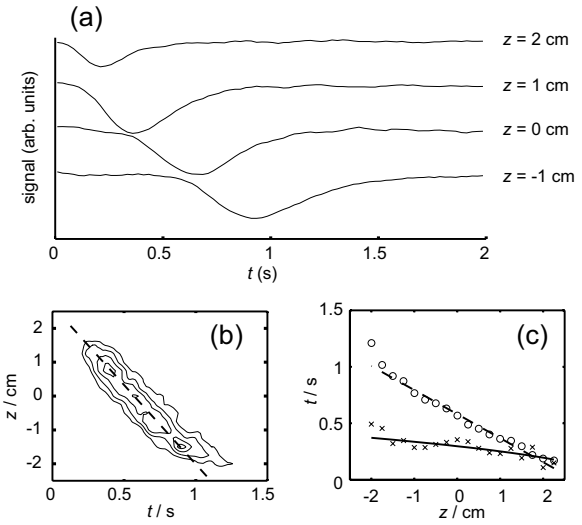

FIG. 2: Visualization of flow and dispersion through a rock sample. (*a*) TOF curves with slice-selective inversion of the spin magnetization along z. The position of the slice with respect to the center of the sample is indicated. The total gas pressure was 3 bar, and the flow rate was 55 slm. (*b*) Contour plot of the TOF curves with z sampled in steps of 2.5 mm. The pressure was 2.5 bar, and the flow rate was 0.50 slm. (*c*) Time of the minimum (○) and width of the dip (×) in the signal as a function of the position of the inverted slice. The data is the same as in (b). The dashed line in (b) and (c) represents the mean velocity, and the full line is a fit of the dispersion of the gas inside the rock as described in the text.

other in order to position both in the homogeneous region of the magnet. RF isolation between the two probes was achieved by a grounded copper shield. The NMR experiments were performed at 300 MHz on a Unity Inova spectrometer (Varian Inc.).

The sample was a Bentheimer sandstone rock, 20 mm in diameter and 39 mm long, with a porosity of 22.5% and pore sizes of about 100 μm. It was inserted into a sealed plastic cocoon and connected to the flow setup using teflon tubes. The flowing gas was a mixture of 1% Xe (natural abundance), 10% N_2, and 89% He. The ^{129}Xe nuclear spin polarization was optically enhanced [22, 23] to about 10% using a XenoSpin polarizer (Amersham Health, Durham, NC). The gas flow rate was controlled between 0.4 and 0.8 slm (standard liter per minute) by two valves – one at the outlet of the polarizer, and the other after the detection probe.

Figure 2a shows the TOF signal as a function of the time t between encoding and detection. For encoding, the ^{129}Xe magnetization was inverted in slices of 10 mm thickness perpendicular to the flow direction (z). The signal is constant before any encoded spins reach the detector. It drops as soon as inverted xenon arrive at the detector, and recovers to its maximum value once all the encoded gas has passed through. For each trace, the field gradient was kept constant while the RF frequency was changed to select different slices. Since the slice at 2 cm is at the outlet of the sample the inverted spins from that slice reach the detector significantly earlier than other slices closer to the sample inlet.

Figure 2b shows a contour plot of the TOF data of an identical experiment, but with slice thickness of 2.5 mm. The slope of this pattern represents the constant mean velocity of the gas flow in the rock, which was 4.7 cm/s as indicated by the line. The position of the minimum and the width of the dips of the TOF data are shown in Figure 2c. The time of the minimum shows an approximate linear dependence on z, indicative of the constant flow velocity. The width of the dip is broadened significantly for slices that are farther away from the detector. For these slices, the gases have traveled a longer distance to the detector compared to the slices near the exit. This broadening is due to hydrodynamic dispersion [24]. In the long time limit, the width is approximately $\sqrt{2Kt}$, giving a dispersion coefficient $K \approx 0.3$ cm^2/s, significantly larger than the xenon diffusion constant $D_0 = 0.1$ cm^2/s in our gas mixture. It is likely that heterogeneity over multiple pore scales is responsible for this large K, since dispersion due to diffusion [24] within the single pore channel alone could not account for $K \sim 0.3$ cm^2/s in our sample. The large D_0 of xenon gas provides a unique opportunity to study dispersion at low Péclet numbers, that is a particularly important regime to explore stagnant zones that upset the well-known theories for dispersion in porous media [25].

The inversion experiment discussed above does not resolve the two transverse dimensions. When the flow pattern is not uniform within the slice owing to, for instance, structural heterogeneity, it is desirable to image

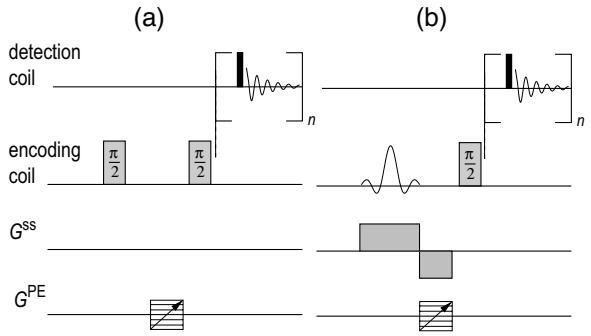

FIG. 3: Remote detection methods using phase encoding. (a) Gradient pulses in three directions, G^{PE}, provide 3D modulation of the spin magnetization. The second $\pi/2$ pulse stores the magnetization along the applied field. (b) Sequence for slice-selective phase-encoding. The bipolar gradient G^{ss} is used for slice selection in one dimension, while phase encoding gradient pulses G^{PE} are used to resolve the other two spatial dimensions. In both methods, detection is done by a train of pulses whose spacing defines the time resolution of the TOF experiment.

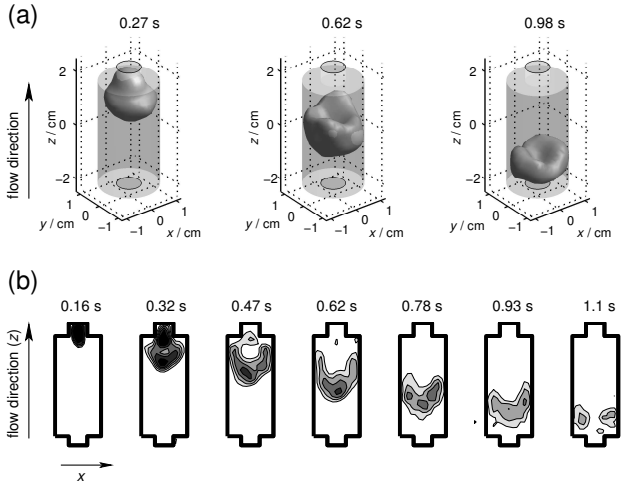

FIG. 4: Images of gas flow through the rock sample. The flow rate was 0.65 slm, and the pressure was 3.7 bar. (a) 3D representation of an isochronal surface at different times after the encoding step (indicated above each image). The cylindrical gray surface represents the sample. A 3D phase encoding sequence with hard encoding pulses was used. The resolution in all three dimension was 0.46 cm. The experiment time was 36 min. (b) TOF x-z images with different detection time after encoding. A slice of 0.75 cm thickness through the center of the rock was excited perpendicular to y, while x and z were resolved with 0.33 cm resolution using phase encoding. The experiment time was 13 min.

the flow in all three dimensions. Three-dimensional (3D) spatial encoding can be done in two ways. The first method achieves 3D imaging in a slice-by-slice fashion and acquires signals for many different slices by systematically scanning the RF frequency and the direction of the field gradient. This method is similar to the projection-reconstruction method introduced by Lauterbur [26].

A second method for 3D resolution uses phase encoding [15], as shown in Fig. 3a. Magnetization is first rotated into the plane perpendicular to the applied magnetic field. Then, a magnetic field gradient pulse is applied which modulates the magnetization by a spatially dependent phase. One component of the precessing magnetization (either sine or cosine of the phase) is then stored along the applied field. Remaining transverse magnetization dephases quickly, while the sensor medium flows to the detector. Thus, only longitudinal magnetization survives the passage through the sample. The entire Fourier components of the image can be sampled in this fashion by incrementing the gradient amplitude in all three dimensions.

This phase encoding approach works well if a full 3D image is to be acquired, which requires that field gradients along all three spatial dimensions be sampled independently. However, this point-by-point sampling of the spatial dimensions largely determines the total time of an experiment. By using a slice-selective preparation pulse, it is possible to encode a single slice in one dimension, while the other dimensions are imaged with phase encoding (Fig. 3b). This reduces the number of phase encoding steps and, thus, the experimental time to obtain a 2D image. This is especially useful if the sample displays a certain symmetry and imaging the third dimension provides no additional information, for example in case of cylindrical symmetry. The disadvantage is that slice-selective pulses can be considerably longer than hard pulses, which may cause a loss of signal for samples with a short decoherence time or rapid diffusion.

Figure 4a shows three images of an experiment with full 3D phase encoding, detected at times $t = 0.27$, 0.62, and 0.98 s after the encoding step. These images reflect the encoding location of the gas molecules that arrive at time t after encoding at the detector. The left-most image shows the gas near the exit and partly inside the narrow outlet region. The second image is centered approximately in the middle of the sample and further extended in the xy plane compared with the image at $t = 0.27$ s. The right-most image was detected about 1 s after encoding. The signal is from the frontal region of the sample near the inlet. The image at $t = 0.62$ s illustrates a gas distribution that is radially uniform, indicating that the gas spreads uniformly into the entire cross-section quickly after the inlet. The dips in the center of the images for $t = 0.62$ and 0.98 s are likely to be due to the flow characteristics in the exit region of the sample. The gas exiting the sample near the center experiences a significantly shorter path compared to the gas near the perimeter, while their respective longitudinal velocity is alike. As a result, for a given time to the detector, the gas on the center comes from a farther

distance.

A series of 2D x-z images is shown in Figure 4b, obtained by selecting a slice parallel to z through the center of the sample, and with phase encoding along x and z. The times marked above the images are the detection time t after encoding, illustrating a time-resolved representation of the flow pattern. The reduction of the flow diameter is visualized near the exit ($t < 0.32$ s). The boomerang-shaped pattern for $t = 0.47 - 0.93$ s is a 2D representation of the dips in the 3D images discussed above for Fig. 4a. The non-uniformities and the irregularities in the images at the current spatial resolution are likely to be due to the limited signal-to-noise ratio and not a result of heterogeneity in the flow field, which is consistent with the uniformity of this type of rock.

An important factor in TOF experiments is the relative flow resolution, *i.e.* how many independent data points can be obtained from the pore volume V_p of the sample. Thus, a dimensionless flow resolution can be defined as

$$R = V_p/V_d, \tag{1}$$

where V_d is the detector volume. The experiments in Fig. 4 were done with $R \approx 15$. R can also be seen as a measure of how small the voxel size can be made while still resolving the dispersion of the sensor medium.

In conclusion, TOF NMR with remote detection represents a new way to characterize fluid flow through porous media. It combines the sensitivity advantage and increased flexibility of remote detection with the possibility to temporally resolve the flow field. Our experiments have demonstrated the feasibility of this approach, which may make it possible to study fluid flow in large, opaque samples. And finally, by using different sensor fluids of gas or liquid phases with varying pressures or flow rates, different regimes of dispersion can be explored experimentally, allowing further refinement of the understanding of flow in porous media.

The authors would like to thank many for their help: D. Verganelakis for sample preparation, J.A. Seeley, M.P. Moschetti, and L.J. Chavez for experimental assistance, and M. D. Hürlimann for discussions. This work was supported by the Director, Office of Science, Office of Basic Energy Sciences, Materials Sciences and Nuclear Science Divisions, of the U. S. Department of Energy under contract DE-AC03-76SF00098. E. H. is supported by a fellowship from the U. S. Department of Homeland Security under DOE contract number DE-AC05-00OR22750.

* Electronic address: joga@waugh.cchem.berkely.edu

† Present address: Department of Chemistry and Biochemistry, University of California at Santa Barbara, Santa Barbara, CA 93106-9510

‡ Electronic address: ysong@slb.com

[1] B. Blümich, *NMR Imaging of Materials* (Oxford University Press, Oxford, 2000).
[2] C. A. Meriles, D. Sakellariou, H. Heise, A. J. Moulé, and A. Pines, Science **293**, 82 (2001).
[3] T. M. Brill, S. Ryu, R. Gaylor, J. Jundt, D. D. Griffin, Y.-Q. Song, P. N. Sen, and M. D. Hürlimann, Science **297**, 369 (2002).
[4] J. Perlo, V. Demas, F. Casanova, C. A. Meriles, J. A. Reimer, A. Pines, and B. Blümich, Science **Epub before print** (2005).
[5] R. L. Kleinberg and J. A. Jackson, Concepts Magn. Reson. **13**, 340 (2001).
[6] G. Eidmann, R. Savelsberg, P. Blümler, and B. Blümich, J. Magn. Reson. A **122**, 104 (1996).
[7] R. L. Kleinberg, C. Flaum, C. Straley, P. G. Brewer, G. E. Malby, E. T. Peltzer, G. Friederich, and J. P. Yesinowski, J. Geophys. Res. **108**, 2137 (2003).
[8] I. V. Koptyug, S. A. Altobelli, E. Fukushima, A. V. Matveev, and R. Z. Sagdeev, J. Magn. Reson. **147**, 36 (2000).
[9] S. Stapf, K. J. Packer, R. G. Graham, J.-F. Thovert, and P. M. Adler, Phys. Rev. E **58**, 6206 (1998).
[10] B. Manz, P. Alexander, and L. F. Gladden, Phys. Fluids **11**, 259 (1999).
[11] E. Kossel, M. Weber, and R. Kimmich, Solid State Nucl. Magn. Reson. **25**, 28 (2004).
[12] R. W. Mair, R. Wang, M. S. Rosen, D. Candela, D. G. Cory, and R. L. Walsworth, Magn. Reson. Imag. **21**, 287 (2003).
[13] A. Abragam, *Principles of Nuclear Magnetism* (Oxford University Press, Oxford, 1961).
[14] A. J. Moulé, M. M. Spence, S. Han, J. A. Seeley, K. L. Pierce, S. Saxena, and A. Pines, Proc. Natl. Acad. Sci. USA **100**, 9122 (2003).
[15] J. A. Seeley, S. Han, and A. Pines, J. Magn. Reson. **167**, 282 (2004).
[16] P. G. de Gennes, C.R. Acad. Sci. II **295**, 1061 (1982).
[17] M. H. Cohen and K. S. Mendelson, J. Appl. Phys. **53**, 1127 (1982).
[18] P. P. Mitra, P. N. Sen, L. M. Schwartz, and P. Le Doussal, Phys. Rev. Lett. **68**, 3555 (1992).
[19] Y.-Q. Song, S. Ryu, and P. N. Sen, Nature **406**, 178 (2000).
[20] R. Wang, R. W. Mair, M. S. Rosen, D. G. Cory, and R. L. Walsworth, Phys. Rev. E **70**, 026312 (2004).
[21] S. Han, S. Garcia, T. J. Lowery, E. J. Ruiz, J. A. Seeley, L. Chavez, D. S. King, D. E. Wemmer, and A. Pines, Anal. Chem. **in press** (2005).
[22] T. G. Walker and W. Happer, Rev. Mod. Phys. **69**, 629 (1997).
[23] B. M. Goodson, J. Magn. Reson. **155**, 157 (2002).
[24] G. I. Taylor, Proc. Royal Soc. (London) A **219**, 186 (1953).
[25] P. G. de Gennes, J. Fluid Mech. **136**, 189 (1983).
[26] P. C. Lauterbur, Nature **242**, 190 (1973).